

A SPECTRAL REGULARIZER FOR UNSUPERVISED DISENTANGLEMENT

Aditya Ramesh

Department of Computer Science
New York University
ar2922@cs.nyu.edu

Youngduck Choi

Department of Computer Science
Yale University
youngduck.choi@yale.edu

Yann LeCun

Department of Computer Science
New York University
yann@cs.nyu.edu

ABSTRACT

Generative models that learn to associate variations in the output along isolated attributes with coordinate directions in latent space are said to possess disentangled representations. This has been a recent topic of great interest, but remains poorly understood. We show that even for GANs that do not possess disentangled representations, one can find paths in latent space over which local disentanglement occurs. These paths are determined by the leading right-singular vectors of the Jacobian of the generator with respect to its input. We describe an efficient regularizer that aligns these vectors with the coordinate axes, and show that it can be used to induce high-quality, disentangled representations in GANs, in a completely unsupervised manner.

1 INTRODUCTION

A generative model $G : \mathbb{R}^m \supseteq Z \rightarrow X \subseteq \mathbb{R}^n$ possesses a disentangled representation when it satisfies two important properties (Higgins et al., 2016). The first property is *orthogonality* of the changes in X resulting from perturbations to individual components of a latent variable in Z . Suppose that we are given an output $x \in X$, let $z := G^{-1}(x)$ be the corresponding latent variable, and let $e_i \in Z$ be the i th standard basis vector, for $i \in [1, m]$. This property requires that $\langle G(z + \alpha e_i), G(z + \alpha e_j) \rangle = 0$ for all $\alpha > 0$, whenever $i \neq j$. Here, $\langle \cdot, \cdot \rangle$ denotes inner product. The second property is *interpretability* of the changes in X resulting from these perturbations. Suppose that the process of sampling from the distribution p_{data} modeled by G can be realized by a simulator that is parameterized over a list of independent, scalar-valued factors or attributes. For example, if p_{data} is a distribution over images of human faces, then these attributes might correspond to concepts such as lighting, azimuth, gender, age, and so on. This property is met when $G(z + \alpha e_i)$ results in a change along a single, distinct attribute, for each $i \in [1, m]$. Quantifying the extent to which this property holds is generally challenging.

Classical dimensionality reduction techniques, such as PCA and metric MDS, can be used to obtain a latent representation satisfying the first property. These techniques are guaranteed to faithfully represent the underlying structure only when the data occupy a linear subspace. For many applications of interest, such as image modeling, the data manifold could be a highly curved and twisted surface that does not satisfy this assumption. The Swiss Roll dataset is a simple example for which this is the case: two points with small euclidean distance could have large geodesic distance on the data manifold. Both techniques measure similarity between each pair of points using euclidean distance, so distant outputs in X could get mapped to nearby embeddings in Z . If our goal is to learn a disentangled representation, then a perturbation to a single component of z should result in a change to $G(z)$ solely along one of the underlying factors of the data-generating process. This means that latent space must be organized such that the distance between nearby embeddings reflects intrinsic

distance on the data manifold. In other words, G must learn to model the local geometry of the data manifold for it to satisfy the second property of disentangled representations.

Several methods were developed to address the failure of classical dimensionality reduction techniques to capture this local geometry. Two of them that have been most broadly applied are Isomap (Tenenbaum et al., 2000) and LLE (Roweis & Saul, 2000). The former regards the dataset as a graph whose edge weights are given by euclidean distances, and applies an all-pairs shortest-path algorithm to construct a symmetric matrix D whose entry d_{ij} approximates the geodesic distance between datapoints x_i and x_j . Then, MDS is applied to D to yield a low-dimensional projection. The latter improves computational efficiency by considering only the K nearest neighbors $\{x_j\}_{j \in N(i)}$ of each datapoint x_i , as determined by euclidean distance. Here, $N(i)$ denotes the indices of the K nearest neighbors of x_i . Then, it computes weights $w_i \in \mathbb{R}^K$ that optimally reconstruct x_i from a linear combination of its neighbors. This process can be stated as an optimization problem involving the local covariance matrix C_i obtained from the centered datapoints $\{x_j - x_i\}_{j \in N(i)}$. Finally, these weights are used to compute a low-dimensional embedding, using a procedure similar to MDS. Both methods seek to transfer geometrical aspects of the data manifold to the low-dimensional embedding space.

We propose using the instantaneous change of the generator to model this local geometry. If the generator is able to produce diverse and realistic samples after training, then the manifold consisting of its outputs should closely approximate the data manifold. We use this fact to construct a measure of distance in output space. First, we consider two outputs x_0 and x_1 , with corresponding latent variables $z_0 := G^{-1}(x_0)$ and $z_1 := G^{-1}(x_1)$, and set $w := x_1 - x_0$. Previous methods such as LLE use euclidean distance as a measure of local proximity, but it may correlate poorly with perceptual similarity (Wang et al., 2004). Part of the reason for this is that all differences along individual pixels receive equal weighting. But perceptual similarity may be impacted more drastically by differences in some regions of an image than in others. Ideally, we would like to assign more importance to the projections of w onto directions from x_0 along which the data manifold experiences large changes, and less importance to the projections of w onto other directions.

The directions from x_0 along which the magnitude of the instantaneous change of the generator is largest are given by the left-singular vectors of the Jacobian respect to its input. First, we note that the instantaneous change of the generator from z_0 along w is given by $J_G(z_0)^t w$, where $J_G(z_0) \in \mathbb{R}^{n \times m}$ is the Jacobian of the generator evaluated at z_0 . Letting $J_G(z_0) = U\Sigma V^t$ be the singular value decomposition of $J_G(z_0)$, we see that

$$\|J_G(z_0)^t w\|^2 = \|V\Sigma U^t w\|^2 = \|\Sigma U^t w\|^2 = \sum_{i \in [1, m]} \sigma_i^2 \langle w, u_i \rangle^2, \quad (1)$$

where σ_i is the i th largest singular value, and u_i is the associated left-singular vector. The larger the projection of w onto the leading left-singular vectors of $J_G(z_0)$, the larger the magnitude of the instantaneous change. On the other hand, if w lies mostly in the span of the trailing left-singular vectors, then the magnitude of the instantaneous change will be small. If G closely approximates the data manifold, then the left-singular vectors should correspond to directions along which the points on the data manifold change most rapidly. Second, we note that the RHS of Equation 1 is a seminorm involving the positive semidefinite matrix $M_x(z_0) := J_G(z_0)J_G(z_0)^t \in \mathbb{R}^{n \times n}$. Its role is analogous to that of the local covariance matrices C_i computed by LLE: both approximate the local geometry of the data manifold. While LLE transfers the properties of C_i to the embedding space using the reconstruction weights, we use the relationship between the left- and right-singular vectors of $J_G(z_0)$.

Our main contributions are as follows:

1. We show that the right-singular vectors can be used to obtain a local disentangled representation about a neighborhood of a given latent variable $z_0 \in Z$;
2. We show that following the path determined by a leading right-singular vector in the latent space of a GAN yields local changes to the output along isolated attributes; and
3. We describe a regularizer that induces disentangled representations in GANs, by aligning the top k right-singular vectors v_1, \dots, v_k with the first k coordinate directions, e_1, \dots, e_k .

2 RELATED WORK

To date, the two most successful approaches for unsupervised learning of disentangled representations are the β -VAE (Higgins et al., 2016) and InfoGAN (Chen et al., 2016). The former proposes increasing the weight β for the KL-divergence term in the objective of the VAE (Kingma & Welling (2013), Rezende et al. (2014)), which is normally set to one. This weight controls the tradeoff between minimizing reconstruction error, and minimizing the KL-divergence between the approximate posterior and the prior of the decoder. The authors observe that as the KL-divergence is reduced, more coordinate directions in the latent space of the decoder end up corresponding to disentangled factors. To measure the extent to which this occurs, they describe a disentanglement metric score, which we use in Section 6. Follow-up work (Burgess et al., 2018) analyzes β -VAE from the perspective of information channel capacity, and describes principled way of controlling the tradeoff between reconstruction error and disentanglement. Several variants of the β -VAE have also since been developed (Kim & Mnih (2018), Chen et al. (2018), Esmaeili et al. (2018)).

InfoGAN (Chen et al., 2016) augments the GAN objective (Goodfellow et al., 2014) with a term that maximizes the mutual information between the generated samples and small subset of latent variables. This is done by means of an auxiliary classifier that is trained along with the generator and the discriminator. Adversarial training offers the potential for a high degree of realism that is difficult to achieve with models like VAEs, which are based on reconstruction error. However, InfoGAN finds fewer disentangled factors than VAE-based approaches on datasets such as CelebA (Liu et al., 2015) and 3DChairs (Aubry et al., 2014), and offers limited control over each latent factor (e.g., maximum rotation angle for azimuth). The mutual information regularizer also detriments sample quality. Hence, the development of an unsupervised method for learning disentangled representations with GANs, while meeting or exceeding the quality of those found by VAE-based approaches, remains an open problem.

Our work makes an important step in this direction. In contrast to previous approaches, which are based on information theory, we leverage the spectral properties of the Jacobian of the generator. This new perspective not only allows us to induce high-quality disentangled representations in GANs, but also to find curved paths over which disentanglement occurs, for GANs that do not possess disentangled representations.

3 IDENTIFYING LOCAL DISENTANGLED FACTORS

The left-singular vectors of $J_G(z_0)$ form an orthonormal set of directions from $x_0 := G(z_0)$ along which the magnitudes of the instantaneous changes in G from z_0 are largest. The perturbations from z_0 that result in instantaneous changes to $G(z_0)$ along these directions are given by the right-singular vectors of $J_G(z_0)$. To see this, we first note that

$$\lim_{\epsilon \rightarrow 0} \frac{G(z_0 + \epsilon v) - G(z_0)}{\epsilon} = J_G(z_0)v. \quad (2)$$

This directional derivative measures the instantaneous change in G resulting from a perturbation of v from z_0 . The magnitude of this change is given by

$$\|J_G(z_0)v\| = (v^t J_G(z_0)^t J_G(z_0)v)^{1/2} =: (v^t M_z(z_0)v)^{1/2} =: n_z(v, z_0),$$

which is a seminorm involving the positive semidefinite matrix $M_z(z_0) := J_G(z_0)^t J_G(z_0) \in \mathbb{R}^{m \times m}$. The unit-norm perturbation from z_0 that maximizes $n_z(v, z_0)$ is given by

$$v_1 := \max_{v \in \mathbb{S}^{m-1}} n_z(v, z_0) = \max_{v \in \mathbb{S}^{m-1}} v^t J_G(z_0)^t J_G(z_0)v, \quad (3)$$

where $\mathbb{S}^{m-1} \subset \mathbb{R}^m$ is the unit sphere. This is the first eigenvector of $M_z(z_0)$, which coincides with the first right-singular vector of $J_G(z_0)$. It follows from the singular value decomposition of $J_G(z_0)$ that the first left-singular vector is given by $u_1 = \sigma_1^{-1} J_G(z_0)v_1$, where σ_1 is the first singular value. Hence, a perturbation from z_0 along v_1 results in an instantaneous change in $G(z_0)$ along u_1 .

Next, we consider the unit-norm perturbation orthogonal to v_1 that maximizes $n_z(v, z_0)$, which is given by

$$v_2 := \max_{v \in \mathbb{S}^{d-1} \cap \text{span}(v_1)^\perp} v^t J_G(z_0)^t J_G(z_0)v. \quad (4)$$

This is the second eigenvector of $M_z(v, z_0)$, which coincides with the second right-singular vector of $J_G(z_0)$. As before, we get $u_2 = \sigma_2^{-1} J_G(z_0) v_2$, where σ_2 is the second singular value. So a perturbation from z_0 along v_2 results in an instantaneous change in $G(z_0)$ along u_2 . Continuing in this way, we consider the k th unit-norm perturbation orthogonal to v_1, \dots, v_{k-1} that maximizes $n_z(v, z_0)$, for each $k \in [2, r]$, where $r := \text{rank}(M_z(z_0))$. This shows that the right-singular vectors of $J_G(z_0)$ result in instantaneous changes to $G(z_0)$ along the corresponding left-singular vectors.

We can use the right-singular vectors of $J_G(z_0)$ to define a local generative model about z_0 . Consider the function $\bar{G}_{z_0} : \mathbb{R}^r \rightarrow \mathbb{R}^n$,

$$\bar{G}_{z_0} : \alpha \mapsto G \left(z_0 + \sum_{i \in [1, r]} \alpha_i v_i \right).$$

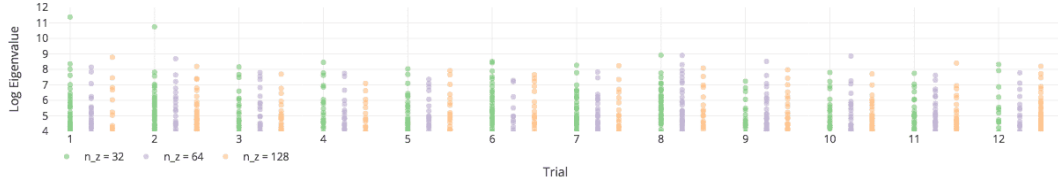
The components of α control perturbations along orthonormal directions, and these directions also result in orthonormal changes to $G(z_0)$. Hence, \bar{G}_{z_0} satisfies the first property for a generative model to possess a disentangled representation, but only about a neighborhood of z_0 . Figure 1 investigates whether \bar{G}_{z_0} also satisfies the second property: interpretability of changes to individual components of α . We can see that perturbations along the leading eigenvectors $M_z(z_0)$, especially the principal eigenvector, often result in the most drastic changes. These changes are interpretable, and tend to make modifications to isolated attributes of the face. To see this in more detail, we consider the top two rows of Figure 1(g). Movement along the first two eigenvectors changes hair length and facial orientation; movement along the third eigenvector decreases the length of the bangs; movement along the fourth and fifth eigenvectors changes background color; and movement along the sixth and seventh eigenvectors changes hair color.

4 FINDING QUASI-DISENTANGLLED PATHS

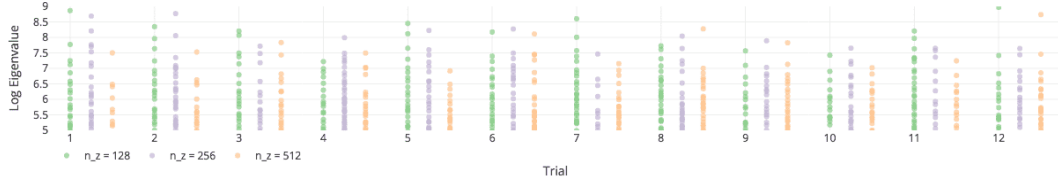
Generative models known to possess disentangled representations, such as β -VAEs (Higgins et al., 2016), allow for continuous manipulation of attributes via perturbations to individual coordinates. Starting from a latent variable $z_0 \in Z$, we can move along the path $\gamma : t \mapsto z_0 + te_i$ in order to vary a single attribute of $G(z_0)$, while keeping the others held fixed. GANs are not known to learn disentangled representations without modifications to the training procedure. Nonetheless, the previous section shows that the local generative model \bar{G}_{z_0} does possess a disentangled representation, but only about a neighborhood of the base point z_0 . We explore whether it is possible to extend this local model to obtain disentanglement along a continuous path from z_0 . To do this, we construct a trajectory $\gamma_k : \mathbb{R} \rightarrow \mathbb{R}^n$, $t \mapsto G(\gamma_k(t))$ by repeatedly following the k th leading eigenvector of $M_z(\gamma_k(t))$, where $\gamma(0) := z_0$. The procedure used to do this is given by Algorithm 1.

We first test the procedure on a toy example for which it is possible to explicitly plot the trajectories. We use the dSprites dataset (Matthey et al., 2017), which consists of 64×64 white shapes on black backgrounds. Each shape is completely determined by six attributes: symbol (square, ellipse, or heart), scale (6 values), rotation angle from 0 to 2π (40 values), and x - and y -positions (30 values each). We trained a GAN on this dataset using a latent variable size of three, fewer than the six latent factors that determine each shape. Figure 2 shows that outputs of the generator along these trajectories vary locally along only one or two attributes at a time. Along the first trajectory γ_1 , the generator first decreases the scale of the square, then morphs it into a heart, increases the scale again, and finally begins to rotate it. Similar comments apply to the other two trajectories, γ_2 and γ_3 .

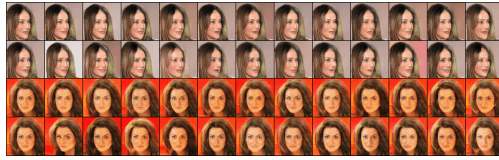
Next, we test the procedure on a GAN trained on the CelebA dataset (Liu et al., 2015) at 64×64 resolution. Figure 3(a) shows the trajectories γ_1 starting at four fixed embeddings z_1, \dots, z_4 . Although the association between the ordinal k of the eigenvector v_k and the attribute of the image being varied is not consistent throughout latent space, local changes still tend to occur along only one or two attributes at a time. Figure 3(b) shows the trajectories $\gamma_1, \gamma_2, \gamma_3$ and γ_5 , all starting from the same fixed embedding z_5 . As is the case for the dSprites dataset, we can see that trajectories γ_k for distinct k tend to effect changes to $G(z_0)$ along distinct attributes. These results suggest that, along trajectories from z_0 determined by a leading eigenvector of $M_z(z_0)$, changes in the output tend to occur along isolated attributes.



(a) Log spectra for CelebA models with $n_f = 64$ and m varied.



(b) Log spectra for LSUN Bedroom models with $n_f = 256$ and m varied.



(c) CelebA ($m = 32, n_f = 64, \epsilon = 0.40$), embeddings z_{10}, z_{11} .



(d) LSUN Bedroom ($m = 128, n_f = 64, \epsilon = 0.80$), embeddings z_5, z_{12} .



(e) CelebA ($m = 64, n_f = 64, \epsilon = 0.65$), embeddings z_6, z_{12} .



(f) LSUN Bedroom ($m = 256, n_f = 64, \epsilon = 0.80$), embeddings z_6, z_8 .



(g) CelebA ($m = 128, n_f = 64, \epsilon = 0.80$), embeddings z_7, z_9 .



(h) LSUN Bedroom ($m = 512, n_f = 64, \epsilon = 0.80$), embeddings z_8, z_{10} .

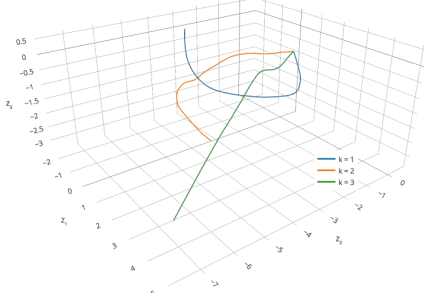
Figure 1: Effect of perturbing a latent variable z along the leading eigenvectors of $M_z(z)$. Subfigures (a) and (b) show the top eigenvalues of $M_z(z_i)$, where $\{z_1, \dots, z_{12}\}$ are fixed embeddings; small eigenvalues are omitted. Subfigures (c)–(d) compare the effects of perturbations along random directions to perturbations along leading eigenvectors. Each subfigure consists of two stacked two-row grids. The leftmost images of each grid are both identical and equal to $G(z_i)$, for some $i \in [1, 12]$. The first row shows the effect of perturbing z_i along 13 directions sampled uniformly from the sphere of radius ϵ , while the second row shows the effect of perturbing z_i along the first 13 leading eigenvectors of $M_z(z_i)$, by the same distance ϵ . Details regarding the model architectures are given in Appendix C.

5 ALIGNING THE LOCAL DISENTANGLED FACTORS

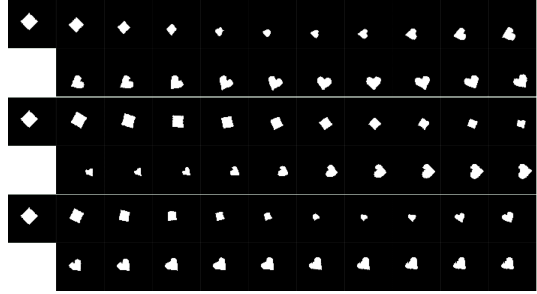
The β -VAE (Higgins et al., 2016) is known to learn disentangled representations, so that traveling along paths of the form

$$\gamma : t \mapsto z_0 + t e_j, \quad (5)$$

for certain coordinate directions e_j , produces changes to isolated attributes of $G(z_0)$. In the previous section, we saw that such paths still exist for GANs, but they are not simply straight lines oriented along



(a) Plots of the trajectories $\{\gamma_k\}_{k \in [1,3]}$.



(b) Outputs of G at iterates $0, 100, \dots, 1000$ of each trajectory γ_k , for $k \in [1, 3]$, from top to bottom, respectively.

Figure 2: Trajectories obtained by following the first three eigenvectors of $M_z(z_0)$ from a fixed embedding $z_0 \in \mathbb{R}^3$ in the latent space of a GAN trained on the dSprites dataset (Matthey et al., 2017). The parameters used for Algorithm 1 are given by $\alpha, \rho, N = 5 \cdot 10^{-3}, 0.99, 2000$. Details regarding the model architecture are given in Appendix C.

Algorithm 1 Procedure to trace path determined by k th leading eigenvector.

Require: $\text{mv} : \mathbb{R}^m \times \mathbb{R}^m \rightarrow \mathbb{R}^d, z, v \mapsto M_z(z)v$ is a function that computes matrix-vector products with the implicitly-defined matrix $M_z(z) \in \mathbb{R}^{m \times m}$.

Require: $z \in \mathbb{R}^m$ is the embedding from which to begin the trajectory.

Require: $k \in [1, m]$ is ordinal of the eigenvector to trace, with $k = 1$ corresponding to the leading eigenvector.

Require: $\alpha > 0$ is the step size.

Require: $\rho \in [0, 1)$ is the decay factor.

Require: $N \geq 1$ is the required number of steps in the trajectory.

```

1
2 procedure TRACEEIGENPATH( $\text{mv}, z, k, \alpha, \rho, N$ )
3    $z_0 \leftarrow z$ 
4   for  $i \in [1, N]$  do
5      $M_z(z) \leftarrow \text{EVALUATENORMALJACOBIAN}(\text{mv}, z)$             $\triangleright$  Details in Appendix A
6      $V, D, V^t \leftarrow \text{SVD}(M_z(z))$ 
7      $w_i \leftarrow v_k$                                                $\triangleright$  Take the  $k$ th eigenvector
8     if  $i \geq 2$  then
9       if  $\langle w_{i-1}, w_i \rangle < 0$  then
10       $w_i \leftarrow -w_i$             $\triangleright$  Prevent backtracking by ensuring that  $\angle(w_{i-1}, w_i) \leq \pi/2$ 
11       $w_i \leftarrow \rho w_{i-1} + (1 - \rho) w_i$             $\triangleright$  Apply decay to smoothen the trajectory
12       $z_i \leftarrow z_{i-1} - \alpha w_i$ 
13   return  $\{z_0, \dots, z_N\}$ 

```

the coordinate axes (see Figure 2). We develop an efficient regularizer that encourages these paths to take the form of Equation 5, based on alignment of the top k eigenvectors of $M_z(z_0)$ with the first k coordinate directions e_1, \dots, e_k . Before proceeding, we describe a useful visualization technique to help measure the extent to which this happens. Let $M_z(z_0) = VDV^t$ be the eigendecomposition of $M_z(z_0)$, where V is an orthogonal matrix whose columns are eigenvectors, and D the diagonal matrix of nonnegative eigenvalues, sorted in descending order. Now we define $\tilde{V} : z \mapsto V$ to be the function that maps z to the corresponding eigenvector matrix V , and let

$$F := \mathbb{E}_{z \sim p_z} \tilde{V}(z) \circ \tilde{V}(z), \quad (6)$$

where p_z is the prior over Z , and ‘ \circ ’ denotes Hadamard product. If the k th column is close to a one-hot vector, with values close to zero everywhere except at entry j , then we know that on average, the k th leading eigenvector of $M_z(z)$ is aligned with e_j . A heatmap generated from this matrix therefore allows us to gauge the extent to which each eigenvector v_k is aligned with the coordinate



(a) Trajectories corresponding to the principal eigenvector for embeddings z_1, \dots, z_4 , from top to bottom, respectively. For embeddings z_1, z_2 , and z_3 , we show iterates $0, 20, \dots, 180$, and for embedding z_4 , we show iterates $0, 10, \dots, 90$. The first trajectory varies azimuth; the second, gender; the third, hair length; and the fourth, hair color.



(b) Trajectories corresponding to the first, second, third, and fifth leading eigenvectors of embedding z_5 , from top to bottom, respectively. We show iterates $0, 20, \dots, 200$. The first trajectory primarily varies azimuth; the second, gender; the third, age; and the fourth, hair color and presence of facial hair.

Figure 3: Trajectories found by following leading eigenvectors from five fixed embeddings z_1, \dots, z_5 , using Algorithm 1 ($\alpha = 1.5 \cdot 10^{-2}, \rho = 0$). Details regarding the model architecture are given in Appendix C.

direction e_k . Figure 5 shows that this does not happen automatically for a GAN, even when it is trained with a small latent variable size. Interestingly, eigenvector alignment does occur for β -VAEs. Appendix B explores this connection in more detail.

We begin by considering the case where we only seek to align the leading eigenvector $v_1 \in \mathbb{R}^m$ with the first coordinate direction $e_1 \in \mathbb{R}^m$. A simple way to do this is to obtain an estimate \hat{v}_1 for v_1 using T power iterations, and then renormalize $\hat{v}_1 \in \mathbb{R}^m$ to a unit vector. We can then maximize the value of the first component of the elementwise squared vector $\hat{v}_1 \circ \hat{v}_1$, and minimize values of the remaining components. Using the mask $s_1 := (-1, 1, \dots, 1) \in \mathbb{R}^m$, we define the regularizer $R_1 : \mathbb{R}^m \rightarrow \mathbb{R}$,

$$R_1(z) := \sum_{i \in [1, m]} (s_1 \circ \hat{v}_1 \circ \hat{v}_1)_i. \quad (7)$$

Since \hat{v}_1 is constrained to unit norm, this regularizer is bounded. It can be incorporated into the loss for the generator using an appropriate penalty weight $\lambda > 0$.

Next, we consider the case where we would like to align the first two leading eigenvectors $v_1, v_2 \in \mathbb{R}^m$ with the first two coordinate directions $e_1, e_2 \in \mathbb{R}^m$. One potential approach is to first compute an estimate \hat{v}_1 to v_1 using T power iterations, as before. Then, we could apply a modified version of the

Algorithm 2 Procedure to estimate the top k eigenpairs of $M_z(z)$.

Require: $\text{mv} : \mathbb{R}^m \rightarrow \mathbb{R}^m$ is a function that computes matrix-vector products with the implicitly-defined matrix $M_z(z) \in \mathbb{R}^{m \times m}$.

Require: $V \in \mathbb{R}^{m \times k}$ is a matrix whose columns are the initial estimates for the eigenvectors.

Require: $T \geq 1$ is the required number of power iterations.

```

1
2  $\epsilon \leftarrow 10^{-8}$                                  $\triangleright$  Guards against division by numbers close to zero
3
4 procedure ESTIMATELEADINGEIGENPAIRS( $\text{mv}, V, T$ )
5   Let  $M_k \in \mathbb{R}^{m \times k}$  be given by Equation 11
6    $V_0 \leftarrow M_k \circ V$                                  $\triangleright$  ‘ $\circ$ ’ denotes Hadamard product
7
8   for  $i \in [1, T]$  do
9      $V_i \leftarrow M \circ \text{mv}(V_{i-1})$ 
10     $\Lambda_i \leftarrow \text{diag}(\text{COLUMNNORMS}(V_i))$ 
11     $V_i \leftarrow V_i (\Lambda_i + \epsilon I)^{-1}$                  $\triangleright$  Renormalize columns
12   return  $\Lambda_T, V_T$ 
13
14 procedure COLUMNNORMS( $A$ )                                 $\triangleright A \in \mathbb{R}^{p \times q}$ 
15   return  $(\|a_1\|, \dots, \|a_q\|)$                           $\triangleright a_i \in \mathbb{R}^p$  is the  $i$ th column of  $A$ 

```

power method to obtain an estimate \hat{v}_2 for v_2 , in which we project the result of each power iteration onto $\text{span}(\hat{v}_1)^\perp$ using the projection $P_1 := I - \hat{v}_1 \hat{v}_1^t$. There are two problems with this approach. Firstly, it could be inaccurate: unless $\|v_1 - \hat{v}_1\| < \tau$ for sufficiently small $\tau > 0$, which may require a large number of power iterations, P_1 will not be an accurate projection onto $\text{span}(v_1)^\perp$. Error in approximating v_1 would then jeopardize the approximation to v_2 . Second, the approach is inefficient. We can only run the power method to estimate v_2 after we have already obtained an estimate for v_1 . If we use T power iterations to estimate each eigenvector, then estimating the first k eigenvectors will require a total of kT power iterations. This is too slow to be practical.

Our specific application of the power method enables an optimization that allows for the k power iterations to be run simultaneously. Once we apply the regularizer to the GAN training procedure, the first eigenvector v_1 will quickly align with the first coordinate direction e_1 . We therefore assume that $v_1 = e_1$. This assumption would imply that $\text{span}(v_1)^\perp = \text{span}(e_2, \dots, e_m)$, so applying P_1 would amount to zeroing out the first component of \hat{v}_2 after each power iteration. Since P_1 would no longer depend on \hat{v}_1 , we can run the power iterations for v_1 and v_2 in parallel. To formally describe this, we let $c_p := 1 \in \mathbb{R}^p$ be the constant vector of ones, and let

$$M_2 := \begin{pmatrix} c_m & 0 \\ & c_{m-1} \end{pmatrix}. \quad (8)$$

Given a matrix $\hat{V}_t^{(2)} \in \mathbb{R}^{m \times 2}$ whose columns are the current estimates for v_1 and v_2 , respectively, we can describe the power iterations for v_1 and v_2 using the recurrence

$$\hat{V}_{t+1}^{(2)} := M_2 \circ (M_z(z_0) \hat{V}_t^{(2)}). \quad (9)$$

Now, let $\hat{V}^{(2)} \in \mathbb{R}^{m \times 2}$ be the final estimate for v_1 and v_2 . To implement the regularizer, we let $s_2 := (1, -1, 1, \dots, 1) \in \mathbb{R}^m$, $S_2 := (s_1 \ s_2) \in \mathbb{R}^{m \times 2}$, and define

$$R_2(z) := \sum_{\substack{i \in [1, m] \\ j \in [1, 2]}} (S_2 \circ \hat{V}^{(2)} \circ \hat{V}^{(2)})_{i,j}. \quad (10)$$

It is straightforward to generalize this approach to the case where we seek to align the first k eigenvectors v_1, \dots, v_k with e_1, \dots, e_k . For each eigenvector v_i , with $i \in [2, k]$, we assume that eigenvectors v_1, \dots, v_{i-1} are already aligned with e_1, \dots, e_{i-1} . The projections onto $\text{span}(e_1)^\perp, \text{span}(e_1, e_2)^\perp, \dots, \text{span}(e_1, \dots, e_{i-1})^\perp$ can be implemented using

Algorithm 3 Procedure to evaluate the alignment penalty.

Require: $k \in [1, d]$ is number of leading eigenvectors to align with e_1, \dots, e_k .
Require: mv, T are as defined in Algorithm 2.

```

1
2 procedure EVALUATE ALIGNMENT REGULARIZER( $k, \text{mv}, T$ )
3   Let  $S_k$  be given by Equation 12
4
5    $\alpha \leftarrow 2/(k(k+1))$ 
6    $A \leftarrow \text{diag}(\alpha \cdot (k, k-1, \dots, 1))$ 
7    $S_k \leftarrow S_k A$             $\triangleright$  Reweight columns to prioritize alignment of leading eigenvectors
8
9    $V_0 \leftarrow \text{RANDOMRADEMACHER}(m, k)$ 
10   $\hat{\Lambda}, \hat{V} \leftarrow \text{ESTIMATELEADINGEIGENPAIRS}(\text{mv}, V_0, t)$ 
11  return  $\text{SUM}(S_k \circ \hat{V} \circ \hat{V})$ 
12
13 procedure RANDOMRADEMACHER( $p, q$ )
14   return  $A \in \mathbb{R}^{p \times q}$ , where  $a_{ij} = 1$  with probability  $1/2$  and  $-1$  with probability  $1/2$ 

```

columns $2, 3, \dots, i$, respectively, of the mask $M_k \in \mathbb{R}^{m \times k}$. This mask, which is a generalization of the one defined by Equation 8, is given by

$$M_k := \begin{pmatrix} 1 & 0 & 0 & 0 & \cdots & 0 \\ 1 & 1 & 0 & 0 & \cdots & 0 \\ 1 & 1 & 1 & 0 & \cdots & 0 \\ 1 & 1 & 1 & 1 & \cdots & 0 \\ \vdots & \vdots & \vdots & \vdots & \ddots & \vdots \\ 1 & 1 & 1 & 1 & \cdots & 1 \\ \vdots & \vdots & \vdots & \vdots & \ddots & \vdots \\ 1 & 1 & 1 & 1 & \cdots & 1 \end{pmatrix} = \begin{pmatrix} c_k & c_k - e_1 & c_k - (e_1 + e_2) & \cdots & c_k - (e_1 + \cdots + e_{k-1}) \\ c_{m-k} & c_{m-k} & c_{m-k} & \cdots & c_{m-k} \end{pmatrix} \in \mathbb{R}^{m \times k}. \quad (11)$$

The resulting procedure to estimate the leading k eigenvectors is described by Algorithm 2. Figure 4 shows that the runtime of Algorithm 2 scales linearly with respect to the number of eigenvectors k and the number of power iterations T . Next, we generalize Equation 10, in order to describe how to evaluate the regularizer R_k . Let $s_p \in \mathbb{R}^m$ be given by $(s_p)_i = -1$ if $i = p$ and 1 otherwise, and define

$$S_k := \begin{pmatrix} -1 & 1 & 1 & \cdots & 1 \\ 1 & -1 & 1 & \cdots & 1 \\ 1 & 1 & -1 & \cdots & 1 \\ \vdots & \vdots & \vdots & \ddots & \vdots \\ 1 & 1 & 1 & \cdots & -1 \\ \vdots & \vdots & \vdots & \ddots & \vdots \\ 1 & 1 & 1 & \cdots & 1 \end{pmatrix} = (s_1 \quad \cdots \quad s_k) \in \mathbb{R}^{m \times k}. \quad (12)$$

Algorithm 3 shows how S_k is used with the result of Algorithm 2 to evaluate R_k .

If the alignment regularizer is implemented exactly as described by Equation 10, it will fail to have the intended effect. The reason for this has to do with the assumption behind the optimization used to run the k power iterations in parallel. Before attempting to align v_i with e_i , we assume that that v_1, \dots, v_{i-1} are already aligned with e_1, \dots, e_{i-1} . When this assumption fails to hold, the projections computed using the columns of M_k will no longer be valid. Figure 5(a) shows that the matrix F does not have a diagonal in its top-left corner, which is what we would expect to see if v_1, \dots, v_k were aligned with e_1, \dots, e_k . Fortunately, there is a simple fix that remedies the situation. We would like to encourage the optimizer to prioritize alignment of v_i with e_i over alignment of v_{i+1}, \dots, v_k with e_{i+1}, \dots, e_k , for all $i \in [1, k-1]$. A simple way to do this is to multiply the i th column of M_k by a weight of $i\alpha$. We choose α based on the condition that these weights sum to one, i.e.,

$$\sum_{i \in [1, k]} i\alpha = 1, \quad \text{implying that} \quad \alpha = \frac{2}{k(k+1)}. \quad (13)$$

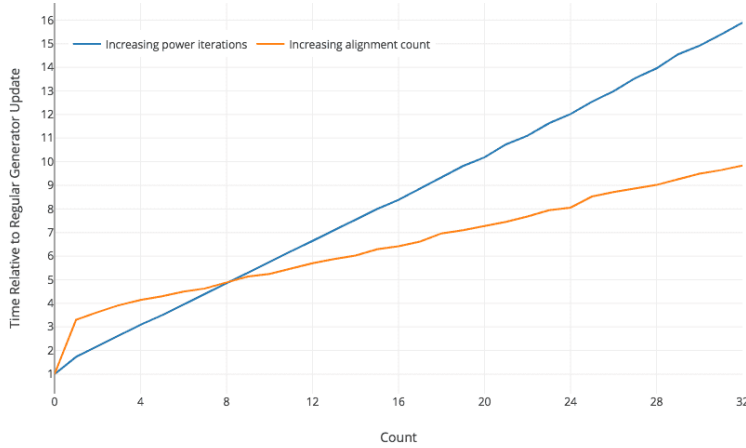


Figure 4: Median relative cost per generator update as a function of the number of eigenvectors k to align, and the number of power iterations T to use for Algorithm 3. The cost is measured relative to the time required to make one RMSProp (Tieleman & Hinton, 2012) update to the parameters of a DCGAN generator (approximately 20.419 ms) with base feature map count 64 and batch size 32. Complete details regarding the model architecture are given in Appendix C. Medians were computed using the update times for the first 500 iterations; the median absolute deviations are small enough as to be indistinguishable from the medians on the plot.

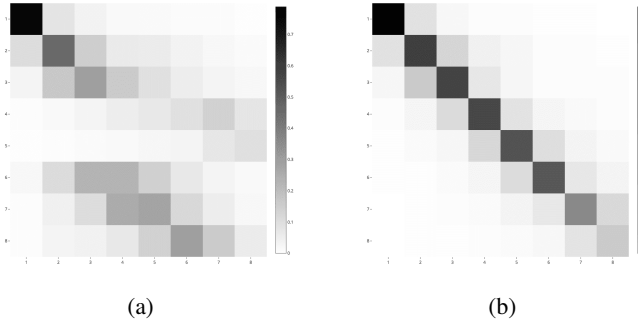


Figure 5: Comparison of the top-left 8×8 corner of the matrix F (Equation 6) for alignment-regularized GANs ($k = 8, T = 8, \lambda = 0.1$), trained with reweighting (left) and without reweighting (right) of the columns of the matrix S_k defined by Equation 12. Both GANs were trained on the CelebA dataset (Liu et al., 2015) at 64×64 resolution, with latent variable size 128. See Appendix C for complete details regarding the model architecture and training procedure.

This reweighting scheme is implemented in lines 5–7 of Algorithm 3. Figure 5(b) confirms that this modification induces the desired structure in the top-left corner of F .

6 RESULTS

We first make a quantitative comparison between our approach and previous methods that have been used to obtain disentangled representations. This requires us to measure the extent to which the second property of disentangled representations – namely, interpretability of changes resulting from perturbations to individual coordinates of a latent variable – holds. Suppose that we had knowledge of the ground truth latent factors for the dataset, along with a simulator that can synthesize new outputs given assignments to these latent factors. Then we could generate pairs of outputs, such that the outputs in each pair differ only along a single attribute. Let (x_0, x_1) be one such pair, and $z_0 := G^{-1}(x_0)$ and $z_1 := G^{-1}(x_1)$ the corresponding latent variables for the generator $G : \mathbb{R}^m \rightarrow \mathbb{R}^n$. If G satisfies

| Model | Disentanglement Score |
|----------------------|-----------------------------------|
| Ground truth | 100 |
| Raw pixels | 45.75 ± 0.8 |
| PCA | 84.90 ± 0.4 |
| ICA | 42.03 ± 10.6 |
| DC-IGN | 99.3 ± 0.1 |
| InfoGAN ¹ | 73.5 ± 0.9 |
| VAE (untrained) | 44.14 ± 2.5 |
| VAE | 61.58 ± 0.5 |
| β -VAE | 99.23 ± 0.1 |
| Ours | 92.34 ± 0.4 |

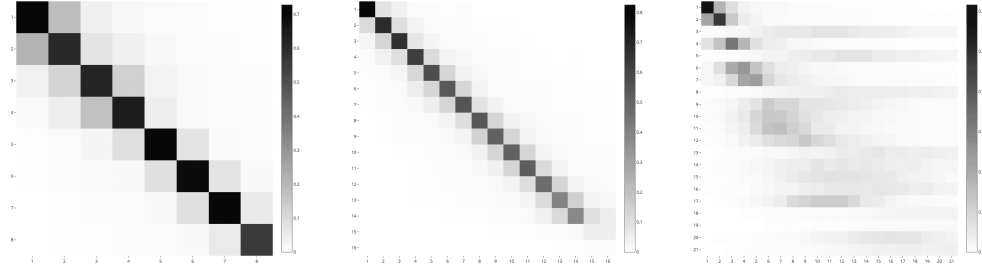
Table 1: Comparison of disentanglement metric scores for our method to those reported in Higgins et al. (2016). We use an alignment-regularized GAN ($k, \lambda = 6, 0.6$) with latent variable size 10. Details regarding the model architecture and training procedure are given in Appendix C.

the second property, then we would expect z_0 and z_1 to be approximately equal along all components, except the one corresponding to the attribute that was varied. Hence, $|z_0 - z_1|$ should be a one-hot vector in expectation. Higgins et al. (2016) propose an evaluation metric based on this idea. It involves training a linear classifier to predict the index of the latent factor that was varied in order to generate each pair. At each step of training for the classifier, we sample a batch of input-target pairs in accordance with the procedure described in (Higgins et al., 2016), and update the classifier using the cross-entropy loss.

Application of the evaluation metric to GANs is complicated by the fact that a direct procedure to invert the generator is usually not available. On the other hand, models such as the β -VAE consist of an encoder that effectively functions as an inverse for the generative model, so this is not an issue. For the purpose of evaluation, we also train an encoder to invert the fixed generator, after GAN training has finished. This additional training procedure uses a standard autoencoding loss, and the details are specified in Appendix D. Table 1 compares our approach to the ones evaluated in (Higgins et al., 2016) on the dSprites dataset (Matthey et al., 2017), which we describe in Section 4. As stated in Appendix C, we added noise to both the real and fake inputs of the discriminator in order to stabilize GAN training on this dataset, for which the pixels are binary-valued. Incorporating this modification into the training procedure for InfoGAN may improve the score reported by (Higgins et al., 2016). Our approach achieves a score competitive to that of DC-IGN, which makes use of supervised information. We also note that we only performed a limited search over the weights $\{0.6, 1.2, \dots, 3.0\}$ for the alignment regularizer, and obtained the best score using a weight of 0.6. We plan to conduct a more thorough search, as well as an investigation into the effect of incorporating noise into the training procedure for InfoGAN, in a future revision.

Next, we make a qualitative comparison between our approach and β -VAE. We train a series of GANs on the CelebA dataset (Liu et al., 2015), with $k \in \{8, 16, 32\}$ for Algorithm 3 and varying values for the alignment regularizer weight λ . We also train a series of β -VAEs with $\beta \in \{1, 2, 4, 8, 16\}$. The results for our method with $k, \lambda = 32, 0.5$ are shown in Figure 7, and the results for β -VAE with $\beta = 8$ in Figure 8. Figure 6 shows the top-left corners of the matrix F given by Equation 6, for three configurations of our approach with $k \in \{8, 16, 32\}$. A penalty weight of $\lambda = 0.5$ was not sufficient to result in a clear diagonal structure in the top-left corner of the matrix F for the configuration with $k = 32$. Nonetheless, this configuration resulted in the largest number of disentangled factors, and the results are shown in Figure 7. The best results for the configurations with $k \in \{8, 16\}$ are shown in Appendix E. We found that the β -VAE configuration with $\beta = 8$ resulted in the largest number of disentangled factors, while still maintaining sufficiently low reconstruction error so as to keep the sample quality acceptable. These results are shown in Figure 8. In addition to better sample quality, our approach is able to learn concepts such as different kinds of hair styles (coordinates 9 and 10 in Figure 7) that are not modeled by the β -VAE.

Even with relatively large values for the penalty weight, the heatmaps shown in Figure 6 contain nonzero entries above and below the diagonal. This can result in some degree of leakage of the



(a) Top-left 8×8 corner of F for GAN with $k, \lambda = 8, 2.3$. (b) Top-left 16×16 corner of F for GAN with $k, \lambda = 16, 1.7$. (c) Top-left 21×21 corner of F for GAN with $k, \lambda = 32, 0.5$.

Figure 6: Comparison of the top-left corners of the matrix F (Equation 6) for alignment-regularized GANs with $k \in \{8, 16, 32\}$. All GANs were trained with latent variable size 128. Details regarding the model architecture and training procedure are given in Appendix C.

attribute controlled by one coordinate into the next. To see this in more detail, we examine the disentangled factors found by the configuration with $k = 16$, which are shown in Figure 12. Coordinates $\{1, 2, 3\}$ all involve change in hair darkness; coordinates $\{4, 5, 6\}$ all involve change in gender; coordinates $\{6, 7, 8, 9\}$ all involve smiling; and coordinates $\{12, 13\}$ all involve change in the location of the hair partition. We identify this as a limitation of our current approach. Modifications to the implementation of the alignment regularizer in Algorithm 3 may help to reduce this leakage. We plan to investigate such improvements in future work.

7 CONCLUSION

Motivated by prior work (Tenenbaum et al. (2000), Roweis & Saul (2000)) on learning embeddings that preserve the geometric structure of the data manifold, we approach disentangled representations from the new perspective of eigenvector alignment. Our method induces disentangled representations in GANs of quality comparable to those obtained by VAE-based approaches (Higgins et al. (2016), Kim & Mnih (2018), Chen et al. (2018), Esmaeili et al. (2018)), without the need to introduce auxiliary models into the training procedure (Chen et al., 2016). Moreover, our method is not specific to the GAN framework (Goodfellow et al., 2014): it could potentially be applied to autoregressive models, such as those used to generate text and audio. We believe this is an important direction for future work. So far, two different perspectives for viewing disentanglement have been proposed: maximizing mutual information and eigenvector alignment. An investigation into the relationship between the two could further our understanding of what disentanglement is and why it occurs.

ACKNOWLEDGEMENTS

We would like to thank for Ryan-Chris Moreno Vasquez and Emily Denton for early discussions that led us to think carefully about the paths determined by the leading eigenvectors of $M_z(z_0)$. We are also grateful for the suggestions provided by Alec Radford, Yuri Burda, and Harri Edwards, which improved the quality of our presentation.

| Coordinate | Description | Example |
|------------|----------------------------|--|
| 1 | Background darkness |  |
| 2 | Azimuth |  |
| 3 | Bangs |  |
| 4 | Gender, bangs, and smiling |  |
| 5 | Smiling |  |
| 6 | Hair color |  |
| 7 | Hair color and hair style |  |
| 8 | Lighting color and bangs |  |
| 9 | Hair color and hair style |  |
| 10 | Hair color and hair style |  |
| 11 | Jawline |  |
| 12 | Smiling and bangs |  |
| 13 | Background color |  |
| 14 | Age and hairline |  |
| 15 | Age |  |
| 17 | Location of hair partition |  |
| 18 | Lighting and skin tone |  |
| 20 | Mouth open |  |
| 21 | Mouth open |  |

Figure 7: Disentanglement results for alignment-regularized GAN ($k, \lambda = 32, 0.5$) with latent variable size 128 on the CelebA dataset, at 64×64 resolution. Details regarding the model architecture and training procedure are given in Appendix C. Results with additional samples for each coordinate can be found at this URL: <https://drive.google.com/open?id=1E7J8wBl2ASqZKqPhMzgQYBs35s1pJBqo>.

| Coordinate | Description | Example |
|------------|---------------------------------|---------|
| 1 | Azimuth | |
| 2 | Background color | |
| 3 | Location of hair partition | |
| 4 | Skin color | |
| 5 | Hair direction | |
| 8 | Background color | |
| 12 | Hair length | |
| 14 | Jawline | |
| 19 | Skin tone | |
| 20 | Hair style | |
| 22 | Sunglasses | |
| 23 | Gender | |
| 25 | Background darkness | |
| 26 | Hairline and skin tone | |
| 28 | Lighting direction and rotation | |
| 32 | Hair size, color, and smiling | |

Figure 8: Disentanglement results for β -VAE ($\beta = 8$) with latent variable size 32 on the CelebA dataset, at 64×64 resolution. Details regarding the model architecture and training procedure are given in Appendix C. Results with additional samples for each coordinate can be found at this URL: <https://drive.google.com/open?id=1NcJ11ceevDxoORM-A9EWUnWCJqVP16cg>.

REFERENCES

Martín Abadi, Paul Barham, Jianmin Chen, Zhifeng Chen, Andy Davis, Jeffrey Dean, Matthieu Devin, Sanjay Ghemawat, Geoffrey Irving, Michael Isard, et al. Tensorflow: A system for large-scale machine learning. In *OSDI*, volume 16, pp. 265–283, 2016.

Mathieu Aubry, Daniel Maturana, Alexei A Efros, Bryan C Russell, and Josef Sivic. Seeing 3d chairs: exemplar part-based 2d-3d alignment using a large dataset of cad models. In *Proceedings of the IEEE conference on computer vision and pattern recognition*, pp. 3762–3769, 2014.

Atilim Gunes Baydin, Barak A Pearlmutter, Alexey Andreyevich Radul, and Jeffrey Mark Siskind. Automatic differentiation in machine learning: a survey. *Journal of Machine Learning Research*, 18(153):1–153, 2017.

Christopher P Burgess, Irina Higgins, Arka Pal, Loic Matthey, Nick Watters, Guillaume Desjardins, and Alexander Lerchner. Understanding disentangling in β -vae. *arXiv preprint arXiv:1804.03599*, 2018.

Tian Qi Chen, Xuechen Li, Roger Grosse, and David Duvenaud. Isolating sources of disentanglement in variational autoencoders. *arXiv preprint arXiv:1802.04942*, 2018.

Xi Chen, Yan Duan, Rein Houthooft, John Schulman, Ilya Sutskever, and Pieter Abbeel. Infogan: Interpretable representation learning by information maximizing generative adversarial nets. In *Advances in neural information processing systems*, pp. 2172–2180, 2016.

Babak Esmaeili, Hao Wu, Sarthak Jain, Alican Bozkurt, N Siddharth, Brooks Paige, Dana H Brooks, Jennifer Dy, and Jan-Willem van de Meent. Structured disentangled representations. *stat*, 1050:29, 2018.

Ian Goodfellow, Jean Pouget-Abadie, Mehdi Mirza, Bing Xu, David Warde-Farley, Sherjil Ozair, Aaron Courville, and Yoshua Bengio. Generative adversarial nets. In *Advances in neural information processing systems*, pp. 2672–2680, 2014.

Irina Higgins, Loic Matthey, Arka Pal, Christopher Burgess, Xavier Glorot, Matthew Botvinick, Shakir Mohamed, and Alexander Lerchner. beta-vae: Learning basic visual concepts with a constrained variational framework. 2016.

Hyunjik Kim and Andriy Mnih. Disentangling by factorising. *arXiv preprint arXiv:1802.05983*, 2018.

Diederik P Kingma and Jimmy Ba. Adam: A method for stochastic optimization. *arXiv preprint arXiv:1412.6980*, 2014.

Diederik P Kingma and Max Welling. Auto-encoding variational bayes. *arXiv preprint arXiv:1312.6114*, 2013.

Ziwei Liu, Ping Luo, Xiaogang Wang, and Xiaou Tang. Deep learning face attributes in the wild. In *Proceedings of International Conference on Computer Vision (ICCV)*, 2015.

Loic Matthey, Irina Higgins, Demis Hassabis, and Alexander Lerchner. dsprites: Disentanglement testing sprites dataset. <https://github.com/deepmind/dsprites-dataset/>, 2017.

Takeru Miyato, Toshiki Kataoka, Masanori Koyama, and Yuichi Yoshida. Spectral normalization for generative adversarial networks. *arXiv preprint arXiv:1802.05957*, 2018.

Alec Radford, Luke Metz, and Soumith Chintala. Unsupervised representation learning with deep convolutional generative adversarial networks. *arXiv preprint arXiv:1511.06434*, 2015.

Danilo Jimenez Rezende, Shakir Mohamed, and Daan Wierstra. Stochastic backpropagation and approximate inference in deep generative models. *arXiv preprint arXiv:1401.4082*, 2014.

Sam T Roweis and Lawrence K Saul. Nonlinear dimensionality reduction by locally linear embedding. *science*, 290(5500):2323–2326, 2000.

Tim Salimans and Diederik P Kingma. Weight normalization: A simple reparameterization to accelerate training of deep neural networks. In *Advances in Neural Information Processing Systems*, pp. 901–909, 2016.

Joshua B Tenenbaum, Vin De Silva, and John C Langford. A global geometric framework for nonlinear dimensionality reduction. *science*, 290(5500):2319–2323, 2000.

T. Tieleman and G. Hinton. Lecture 6.5—RmsProp: Divide the gradient by a running average of its recent magnitude. COURSERA: Neural Networks for Machine Learning, 2012.

Jamie Townsend. A new trick for calculating jacobian vector products. <https://j-towns.github.io/2017/06/12/A-new-trick.html>, 2017.

Zhou Wang, Alan C Bovik, Hamid R Sheikh, and Eero P Simoncelli. Image quality assessment: from error visibility to structural similarity. *IEEE transactions on image processing*, 13(4):600–612, 2004.

Sitao Xiang and Hao Li. On the effects of batch and weight normalization in generative adversarial networks. *stat*, 1050:22, 2017.

A FORWARD- AND REVERSE-MODE AUTOMATIC DIFFERENTIATION

The entries of J_G are not explicitly stored in memory: it is an implicit-defined matrix. As such, information about J_G must be accessed via automatic differentiation (AD), of which there are two kinds: forward-mode and reverse-mode. We briefly describe them here, and refer the reader to (Baydin et al., 2017) for a more comprehensive survey.

Suppose that we are given a differentiable function $f : \mathbb{R}^m \rightarrow \mathbb{R}^n$ corresponding to a feedforward neural network with L layers, and let $G := (V, E)$ be its representation as a computation graph. For each $k \in [1, L]$, let R_k be the set of nodes corresponding to the k th layer, and let $r_k : \mathbb{R}^{\alpha_{k-1}} \rightarrow \mathbb{R}^{\alpha_k}$ be the function computed by the nodes in R_k , with $\alpha_0 := m$ and $\alpha_L := n$. Then $f = r_L \circ r_{L-1} \circ \dots \circ r_2 \circ r_1$. Finally, let $\bar{x} \in \mathbb{R}^m$ denote the variable for the input to f , and $\bar{b}_{k-1} \in \mathbb{R}^{\alpha_{k-1}}$ the variable for the input to r_k , with $\bar{b}_0 := \bar{x}$. Given a vector $v \in \mathbb{R}^m$, forward-mode AD computes Jv . It works according to the recurrence

$$\begin{aligned} v_k &:= (D_{\bar{x}} r_k|_{\bar{x}=\bar{x}}) v = (D_{\bar{b}_{k-1}} r_k|_{\bar{b}_{k-1}=\bar{b}_{k-1}}) (D_{\bar{x}} r_{k-1} \circ \dots \circ r_1|_{\bar{x}=\bar{x}}) v \\ &= (D_{\bar{b}_{k-1}} r_k|_{\bar{b}_{k-1}=\bar{b}_{k-1}}) v_{k-1}, \end{aligned}$$

where $k \in [1, L]$ and $v_0 := v$. After step k , we will have obtained the product of the Jacobian of r_k with respect to x , and v ; after step L , we will have obtained the desired product Jv .

Forward-mode AD computes Jv far more efficiently than the approach of first evaluating J , and subsequently multiplying by v . Suppose for simplicity that $\alpha_k = n$ for all $k \in [0, L]$, so that $J \in \mathbb{R}^{n \times n}$. To compute J independently, we would use the chain rule, which gives

$$D_{\bar{x}} f|_{\bar{x}=\bar{x}} = (D_{\bar{b}_{L-1}} r_L|_{\bar{b}_{L-1}=\bar{b}_{L-1}}) (D_{\bar{b}_{L-2}} r_{L-1}|_{\bar{b}_{L-2}=\bar{b}_{L-2}}) \dots (D_{\bar{b}_0} r_1|_{\bar{b}_0=\bar{x}}).$$

Each layer r_k , for $k \in [1, L]$, must compute its $n \times n$ Jacobian, and each layer after the first must multiply its Jacobian with the $n \times n$ Jacobian of the preceding layer with respect to x . This process is described by the recurrence

$$D_{\bar{x}} r_k|_{\bar{x}=\bar{x}} = (D_{\bar{b}_{k-1}} r_k|_{\bar{b}_{k-1}=\bar{b}_{k-1}}) (D_{\bar{x}} r_{k-1}|_{\bar{x}=\bar{x}}).$$

Assuming that $\Theta(1)$ operations are required to compute each element of the Jacobian, the total number of operations required is proportional to

$$N := n^2 + (L-1)(n^2 + n^3) \in \Theta(n^3),$$

despite the fact that J has only n^2 elements. On the other hand, the k th step of the forward-mode recurrence requires $\Theta(n)$ operations, so computing Jv only requires $\Theta(Ln)$ operations. By running forward-mode with $v = e_i$ for each $i \in [1, n]$, we can form J column-by-column in only $\Theta(Ln^2)$ operations. Henceforth, we will measure operation count in terms of invocations to the AD engine, rather than by counting elementary operations.

Of the two kinds of AD, it is reverse-mode that finds the most use in machine learning. Given a vector $w \in \mathbb{R}^n$, it computes $J^t w$. Most applications involve minimizing a scalar-valued loss function with respect to a vector of parameters, which corresponds to the case where $n = 1$. This special case is otherwise known as backpropagation. Unlike forward-mode, which begins at the first layer and ends at the last, reverse-mode begins at the last layer and ends at the first. It works according to the recurrence

$$\begin{aligned} w_k^t &:= w^t (D_{\bar{b}_{k-1}} r_k|_{\bar{b}_{k-1}=\bar{b}_{k-1}}) = w^t (D_{\bar{b}_k} r_L \circ \dots \circ r_{k+1}|_{\bar{b}_k=\bar{b}_k}) (D_{\bar{b}_{k-1}} r_k|_{\bar{b}_{k-1}=\bar{b}_{k-1}}) \\ &= w_{k+1}^t (D_{\bar{b}_{k-1}} r_k|_{\bar{b}_{k-1}=\bar{b}_{k-1}}), \end{aligned}$$

where k ranges from L to 1, and $w_L := w$. After L steps, we will have obtained the desired product $J^t w$. Machine learning frameworks typically expose the full interface to the reverse-mode AD engine, rather than specializing to the case of backpropagation. E.g., in TensorFlow (Abadi et al.,

```

1 import tensorflow as tf
2
3 def forward_gradients(ys, xs, d_xs):
4     v = tf.placeholder_with_default(tf.ones_like(ys), shape=ys.get_shape())
5     g = tf.gradients(ys, xs, grad_ys=v)
6     return tf.gradients(g, v, grad_ys=d_xs)
7
8 def j_v(ys, xs, vs):
9     return forward_gradients(ys, xs, vs)
10
11 def jt_v(ys, xs, vs):
12     return tf.gradients(ys, xs, vs)
13
14 def jt_j_v(ys, xs, vs):
15     jv = j_v(ys, xs, vs)
16     return tf.gradients(ys, xs, jv)
17
18 def j_jt_v(ys, xs, vs):
19     jt_v_ = jt_v(ys, xs, vs)
20     return forward_gradients(ys, xs, jt_v_)

```

Listing 1: TensorFlow implementation of Jacobian-vector operations.

2016), one can change the value of w for `tf.gradients` from a vector of ones to a custom value specified by the `grad_ys` parameter.

If desired, we can compute the entire Jacobian using either type of AD. By running forward-mode with $v = e_i$ for each $i \in [1, m]$, we can form J column-by-column, using m total invocations to AD. Similarly, by running reverse-mode with $w = e_i$ for each $i \in [1, n]$, we can form J row-by-row using n total invocations to AD. If $n > m$, the former is typically faster; otherwise, the latter is preferable. We note that while AD offers a relatively efficient approach for evaluating J , doing so at each iteration of optimization becomes impractical.

Many popular machine learning frameworks (e.g., TensorFlow) do not implement forward-mode natively, since it is seldom used for machine learning. Surprisingly, this is not a limitation: *reverse-mode can be used to implement forward-mode*. Given a differentiable function $f : \mathbb{R}^m \rightarrow \mathbb{R}^n$, we can compute $w^t J$ for a given vector $w \in \mathbb{R}^n$, using reverse-mode AD. Treating the input to f as a constant, we can regard $w^t J$ as a function $g : \mathbb{R}^n \rightarrow \mathbb{R}^m$, $w \mapsto w^t J$. The derivative of g with respect to w is given by J^t , and so another application of reverse-mode AD allows us to compute $v^t J^t = (Jv)^t$. Hence, reverse-mode AD can be used to implement forward-mode AD. This trick was first described by (Townsend, 2017). We provide a TensorFlow implementation of the procedures to compute Jv , $J^t v$, $J^t Jv$, and $J J^t v$ in Listing 1.

B EIGENVECTOR ALIGNMENT FOR β -VAEs

The results from Section 4 suggest that alignment of the eigenvectors of $M_z(z_0)$ with the coordinate axes might be sufficient to induce disentanglement in the latent representation of a generative model. The β -VAE is known to learn such a representation when β is increased, so that the KL-divergence between the approximate posterior and the prior of the decoder is made sufficiently small. Suppose that a β -VAE exhibits disentanglement along the j th coordinate direction in latent space. Then paths of the form $\gamma : t \mapsto z_0 + te_j$ will produce changes to $G(z_0)$ along isolated factors of variation. If such a path coincides with the trajectory found by Algorithm 1 for the k th leading eigenvector throughout latent space, then this eigenvector must be aligned with the j th coordinate axis. Hence, we would expect the k th column of the matrix F given by Equation 6 to be a one-hot vector close to e_j . Figure 9 shows that, in fact, several columns of F have high similarity to coordinate directions.

Next, we investigate whether a column of F having high similarity with a coordinate direction e_j implies that disentanglement actually occurs along $\gamma : t \mapsto z_0 + te_j$. Figure 10 shows that with the exception of three coordinates having similarity greater than 0.35, this turns out not to be the case. In other words, several of the eigenvectors naturally align with coordinate directions during training, but disentanglement does not reliably occur along all of them. More work needs to be done in order to better understand the relationship between eigenvector alignment and disentangled representations.

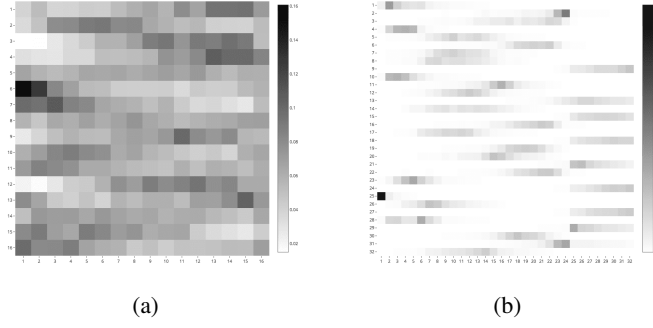


Figure 9: Comparison between the average squared eigenvector matrices F (Equation 6) for a GAN generator with latent variable size 16 (left) and the decoder from a β -VAE ($\beta = 8$) with latent variable size 32 (right), both trained on the CelebA dataset. Complete architecture and training details are provided in Appendix C. The matrix F for the VAE decoder contains several columns that are close to one-hot vectors. By contrast, the same matrix for the GAN generator exhibits little structure, despite the fact that it is trained with a small latent variable size.

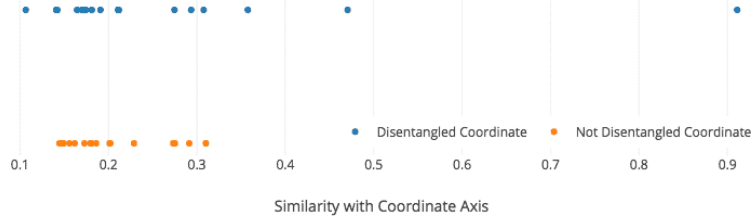


Figure 10: Investigation of whether the matrix F can be used to determine which directions in latent space correspond to disentangled factors for a β -VAE. For each $i \in [1, 32]$, we compute the maximum value along the i th row of matrix F shown in Figure 9(b). Then, we plot a point indicating whether or not disentanglement occurs along this direction, as determined by visual inspection. The directions that do result in disentanglement are shown in Figure 8.

C GENERATOR ARCHITECTURES AND TRAINING PROCEDURE

All models in this work are based on the DCGAN (Radford et al., 2015) architecture. Table 2 describes the architectures of the generator and discriminator (in the case of GANs) and the encoder and decoder (in the case of VAEs) associated with each figure and table. All models use the translated PReLU activation function (Xiang & Li, 2017); the ReLU leaks are learned, and clipped to the interval $[0, 1]$ after each parameter update. The only data preprocessing we applied was to scale the pixel values to the interval $[0, 1]$. The GANs were trained using the original, non-saturating GAN loss described in Goodfellow et al. (2014) with multivariate normal prior. Both the generator and the discriminator were trained using RMSProp (Tieleman & Hinton, 2012) with step size 10^{-4} , decay factor 0.9, and $\epsilon = 10^{-6}$. Each parameter update was made using a batch size of 32, and the models were trained for a total of 750,000 updates. The VAEs were trained using a gaussian likelihood model for the decoder, and the log-diagonal covariance parameterization for the encoder. The fixed, per-pixel standard deviation of the decoder was chosen such that, disregarding constant terms, the log-likelihood corresponds to the reconstruction error, normalized by the product of the number of channels and the number of pixels. To optimize the evidence lower bound, we used Adam (Kingma & Ba, 2014) with $\beta_1, \beta_2, \epsilon = 0.5, 0.99, 10^{-8}$. Each parameter update was made using a batch size of 32, and the models were trained for a total of 1,500,000 updates. The KL-divergence weight β was increased linearly from 0 to the final value over the first 1,000,000 updates. We applied the function $x \mapsto 2(\tanh(x) + 1/2)$ to the outputs of both the GAN generators and the VAE decoders; this ensures that the output pixel values are in the interval $[0, 1]$. To predict the mean and log-diagonal covariance with the VAE encoders, we apply the translated ReLU activation function (Xiang &

| Figure | DCGAN Base Feature Map Count | Latent Variable Size | Notes |
|---------------------------|------------------------------|----------------------|-------|
| 1(c) | 64 | 32 | 1 |
| 1(e) | 64 | 64 | 1 |
| 1(g) | 64 | 128 | 1 |
| 1(d), 5, 4, 6(a), 6(b), 7 | 64 | 128 | 1 |
| 3, 11, 12 | 128 | 128 | 1 |
| 1(f) | 64 | 256 | 1 |
| 1(h) | 64 | 512 | 1 |
| 2 | 64 | 3 | 1, 3 |
| 1 | 64 | 10 | 1, 3 |
| 9(a) | 64 | 16 | 1 |
| 9(b), 10 | 64 | 32 | 2 |

Table 2: GAN and β -VAE architectures used for all figures and tables. Note 1: weight normalization (Salimans & Kingma, 2016) was applied both to the generator and the discriminator, with the scale g fixed to one for the generator. Note 2: spectral weight normalization (Miyato et al., 2018) was applied both to the encoder and the decoder, with learned scales for both. Note 3: gaussian noise with standard deviation 0.6 was added to both real and fake inputs to the discriminator.

Li, 2017) to the final convolutional features, followed by two fully-connected layers, one for each statistic.

D IMPLEMENTATION DETAILS FOR DISENTANGLEMENT METRIC SCORE

Algorithm 4 describes the procedure used to generate the batches to train and evaluate the classifier for the disentanglement metric (Higgins et al., 2016). We use $n_{\text{inst}}, n_{\text{batch}} = 64, 32$, and update the classifier using SGD with nesterov accelerated gradient (step size 10^{-2} , momentum 0.99). We train the classifier using a total of 10,000 parameter updates, and evaluate its performance using 5000 instances, as reported by (Higgins et al., 2016). To invert the pretrained GAN generator, we train a VAE decoder with twice the base feature map count for the generator, using 30,000 parameter updates. The details for this training procedure are identical to those for regular VAE training described in Appendix C, except that the generator is not updated, and the KL-divergence weight β is set to zero. In other words, we use a standard autoencoding loss with a fixed decoder.

Algorithm 4 Procedure to generate a batch for disentanglement metric classifier.

Require: $n_{\text{inst}} \geq 1$ is the number of aligned pairs to use, in order to create each instance in the batch.
Require: $n_{\text{batch}} \geq 1$ is the batch size.
Require: $\text{Enc} : \mathbb{R}^n \rightarrow \mathbb{R}^m$ is the encoder functioning as the inverse of the generator G .

```
 $c \leftarrow (3, 6, 40, 30, 30)$                                  $\triangleright$  Ranges for the five attributes that determine each shape

procedure SAMPLESHAPE( $i, v$ )                                 $\triangleright$  Sample shape with attribute  $i$  fixed to value  $v$ 
  for  $j \in [1, 5]$  do
     $u_j \leftarrow \text{RANDOMUNIFORM}(1, c_j)$ 
   $u \leftarrow (u_1, u_2, u_3, u_4, u_5)$ 
   $u_i \leftarrow v$ 
  return MAKESHAPE( $u$ )

procedure MAKEINSTANCE( $n_{\text{inst}}$ ,  $\text{Enc}$ )
   $i \leftarrow \text{RANDOMUNIFORM}(2, 5)$                                  $\triangleright$  Sample index of attribute to fix
   $v \leftarrow \text{RANDOMUNIFORM}(1, c_i)$                                  $\triangleright$  Sample value for fixed attribute
   $z \leftarrow 0 \in \mathbb{R}^m$ 
  for  $k \in [1, n_{\text{inst}}]$  do
     $z_0 \leftarrow \text{Enc}(\text{SAMPLESHAPE}(i, v))$ 
     $z_1 \leftarrow \text{Enc}(\text{SAMPLESHAPE}(i, v))$ 
     $z \leftarrow z + |z_0 - z_1|$ 
  return  $z/n_{\text{inst}}, i$ 

procedure MAKEBATCH( $n_{\text{inst}}, n_{\text{batch}}$ ,  $\text{Enc}$ )
  inputs  $\leftarrow \emptyset$ 
  targets  $\leftarrow \emptyset$ 
  for  $k \in [1, n_{\text{batch}}]$  do
     $x, y \leftarrow \text{MAKEINSTANCE}(n_{\text{inst}}, \text{Enc})$ 
    inputs  $\leftarrow \text{inputs} \cup \{x\}$ 
    targets  $\leftarrow \text{targets} \cup \{y\}$ 
  return inputs, targets
```

E ADDITIONAL GAN DISENTANGLEMENT RESULTS

| Coordinate | Description | Example |
|------------|------------------------------------|---------|
| 1 | Background darkness and hair color | |
| 2 | Azimuth, lighting, and hair color | |
| 3 | Hairline and hair color | |
| 4 | Azimuth | |
| 5 | Shadow | |
| 6 | Smiling, age, skin tone, gender | |
| 7 | Smiling, age, jawline | |
| 8 | Jawline and hairstyle | |

Figure 11: Disentanglement results for alignment-regularized GAN ($k, \lambda = 32, 2.3$). Details regarding the model architecture and training procedure are given in Appendix C. Results with additional samples for each coordinate can be found at this URL: https://drive.google.com/open?id=1e3WTSx1wDSk6JC01O9Z7WsJI6g_zbZe2.

| Coordinate | Description | Example |
|------------|--|---------|
| 1 | Background and hair darkness | |
| 2 | Azimuth and hair darkness | |
| 3 | Hair length, hair darkness, and lighting | |
| 4 | Smiling and gender | |
| 5 | Hair length, hair darkness, and gender | |
| 6 | Smiling, bangs, and gender | |
| 7 | Smiling and hairstyle | |
| 8 | Smiling, jawline, and glaring expression | |
| 9 | Smiling, bangs, and mouth open | |
| 10 | Hairline | |
| 11 | Raised eyebrows and skin tone | |
| 12 | Raised eyebrows and location of hair partition | |
| 13 | Raised eyebrows and location of hair partition | |
| 14 | Lighting color | |

Figure 12: Disentanglement results for alignment-regularized GAN ($k, \lambda = 8, 1.7$). Details regarding the model architecture and training procedure are given in Appendix C. Results with additional samples for each coordinate can be found at this URL: <https://drive.google.com/open?id=1s-CZVILzwDU3Y839haDHoPVpqv26tTya>.